Earth and Planetary Science Letters 514 (2019) 48–61

Contents lists available at ScienceDirect

Earth and Planetary Science Letters

www.elsevier.com/locate/epsl

Seismic imaging of Santorini: Subsurface constraints on caldera collapse and present-day magma recharge

E.E.E. Hooft [a,*], B.A. Heath [a], D.R. Toomey [a], M. Paulatto [b], C.B. Papazachos [c], P. Nomikou [d], J.V. Morgan [b], M.R. Warner [b]

[a] Department of Earth Sciences, University of Oregon, USA
[b] Department of Earth Science & Engineering, Imperial College London, UK
[c] Geophysical Laboratory, Aristotle University of Thessaloniki, Greece
[d] Department of Geology and Geoenvironment, National and Kapodistrian University of Athens, Greece

ARTICLE INFO

Article history:
Received 6 January 2019
Accepted 26 February 2019
Available online xxxx
Editor: R. Bendick

Keywords:
caldera formation
magma recharge
Santorini Late Bronze Age (LBA)/Minoan eruption
active source seismic tomography

ABSTRACT

Volcanic calderas are surface depressions formed by roof collapse following evacuation of magma from an underlying reservoir. The mechanisms of caldera formation are debated and predict differences in the evolution of the caldera floor and distinct styles of magma recharge. Here we use a dense, active source, seismic tomography study to reveal the sub-surface physical properties of the Santorini caldera in order to understand caldera formation. We find a ~3-km-wide, cylindrical low-velocity anomaly in the upper 3 km beneath the north-central portion of the caldera, that lies directly above the pressure source of the 2011-2012 inflation. We interpret this anomaly as a low-density volume caused by excess porosities of between 4% and 28%, with pore spaces filled with hot seawater. Vents that were formed during the first three phases of the 3.6 ka Late Bronze Age (LBA) eruption are located close to the edge of the imaged structure. The correlation between older volcanic vents and the low-velocity anomaly suggests that this feature may be long-lived. We infer that collapse of a limited area of the caldera floor resulted in a high-porosity, low-density cylindrical volume, which formed by either chaotic collapse along reverse faults, wholesale subsidence and infilling with tuffs and ignimbrites, phreatomagmatic fracturing, or a combination of these processes. Phase 4 eruptive vents are located along the margins of the topographic caldera and the velocity structure indicates that coherent down-drop of the wider topographic caldera followed the more limited collapse in the northern caldera. This progressive collapse sequence is consistent with models for multi-stage formation of nested calderas along conjugate reverse and normal faults. The upper crustal density differences inferred from the seismic velocity model predict differences in subsurface gravitational loading that correlate with the location of 2011-2012 edifice inflation. This result supports the hypothesis that sub-surface density anomalies may influence present-day magma recharge events. We postulate that past collapses and the resulting topographical and density variations at Santorini influence magma focusing between eruptive cycles, a feedback process that may be important in other volcanoes.

1. Introduction

The mechanisms involved in the formation of volcanic calderas continue to be a matter of some debate, in part due to their structural complexity as revealed by geological field studies. Proposed formational models include multi-event piecemeal collapse (Williams, 1941), piston subsidence of a central plug followed by erosion at the margins (Lipman, 1997; Walker, 1984), nested caldera formation along sets of inward- and outward-dipping ring faults (Roche et al., 2000; Scandone and Acocella, 2007), and funnel-shaped collapse into a cored-out volcanic vent (Aramaki, 1984; Escher, 1929; Yokoyama, 1981). Other clues to caldera formation are provided by sandbox experiments and numerical model predictions of subsurface stress and suggest that, as deformation and evacuation progress, the style of roof collapse evolves from initial reverse faulting to later development of an outer ring of conjugate normal faults (Acocella, 2006; Holohan et al., 2015).

Shallow low-velocity anomalies and caldera faults have previously been seismically imaged beneath volcanoes and, in a few cases, seismicity has been detected along ring faults. At some

* Corresponding author.
E-mail address: emilie@uoregon.edu (E.E.E. Hooft).

https://doi.org/10.1016/j.epsl.2019.02.033
0012-821X/

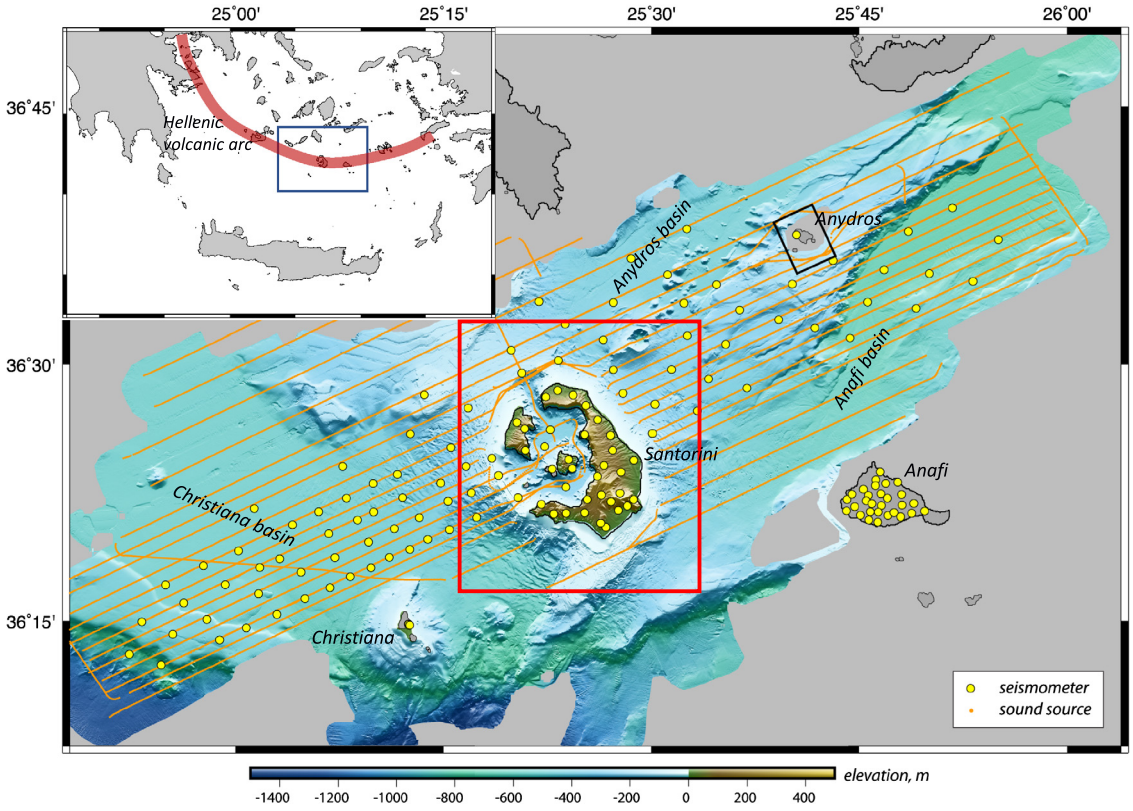

Fig. 1. PROTEUS seismic experiment. Map of the sea bottom and land topography (Hooft et al., 2017) and the layout of the entire marine-land dataset that was collected in November-December of 2015. The dense seismic experiment recorded ~ 14,300 controlled-sound sources (beige dots) from the R/V Marcus Langseth on 90 ocean-bottom and 65 land seismometers (yellow circles). The red rectangle shows the region of this study and the islands and sedimentary basins are labeled. The black rectangle shows the area that was averaged to obtain the velocity-depth curve for the reference metamorphic profile in Fig. 5a. (For interpretation of the colors in the figure(s), the reader is referred to the web version of this article.)

large caldera systems, such as Yellowstone (Farrell et al., 2015) and Campi Flegrei (Vanorio, 2005), these localized low-velocity regions in the uppermost crust (<5 km) are explained as hydrothermal reservoirs. Elsewhere, for example at Krakatoa (Deplus et al., 1995), Deception Island (Zandomeneghi et al., 2009), and Newberry (Beachly et al., 2012; Heath et al., 2015) volcanoes, the caldera is filled with low-velocity material interpreted to correspond to sediments and brecciated caldera-fill. These low-velocity zones narrow downward and connect to magmatic systems in the upper crust below ~2 km depth. At other volcanoes, displacement on caldera ring faults has been inferred from seismicity recorded during diking and eruption episodes. At Bárdarbunga earthquakes beneath the caldera delineate a tall (8-km high), slightly-tilted plug overlying the inferred magma system (Gudmundsson et al., 2016). While at Axial Seamount conjugate inward- and outward-facing faults were activated during inflation and deflation episodes (Wilcock et al., 2016) providing observational evidence that caldera floor morphology can be controlled by conjugate fault structures.

The proposed caldera collapse models predict considerable differences in the structure of the upper portions of volcanoes that may affect the stress state of the edifice and the movement of magma, resulting in distinct styles of magma recharge and post-collapse volcanism. In this paper we use a dense, active source, seismic tomography study of Santorini caldera (Fig. 1) to image the seismic velocity structure of a collapsed caldera at an arc volcano. We interpret the velocity structure in terms of physical properties and then make use of extensive geological studies of the evolution of the volcano and of the latest caldera-forming eruption to explore models that might explain the caldera structure. In addition, we examine how density anomalies beneath the caldera could act to localize present-day magma recharge, specifically in the context of the spatial correlation of caldera structure with a recent episode of volcano inflation.

2. Santorini volcano

Santorini is an arc volcano in the Hellenic subduction zone (Fig. 1) that has been the subject of numerous geological studies over more than a century. In a regional context, Santorini is located within the sedimentary basins and metamorphic horsts of the extended Aegean continental crust. Major explosive activity at Santorini began about 360 ka and included up to 12 large explosive eruptions (Druitt, 2014). It has a history of alternating caldera-forming, explosive, Plinian eruptions and caldera-filling, effusive, shield-building periods. The most recent Plinian event was the explosive Late Bronze Age (LBA) eruption (also known as the Minoan eruption) that formed the present-day caldera 3.6 kyr ago and was followed by effusive dome-building eruptions to create the Kameni islands within the caldera (Fig. 2a).

The following episodes established the geological setting of the LBA eruption. A large intra-caldera shield edifice, the ~350-m-high Skaros-Therasia complex, was built effusively between 67 and 23 ka (Druitt et al., 1999; Heiken and McCoy, 1984). This shield complex collapsed in the Cape Riva explosive eruption at 22 ka (Fabbro et al., 2013) to form a shallow water caldera located in the northern basin of the present-day caldera (Athanassas et al., 2016). Chemical analysis of the stromatolite lithics show that this caldera was a semi-restricted marine bay with no more than a few meters of water depth (Anadón et al., 2013; Friedrich et al., 1988). Subsequent intra-caldera effusive activity constructed the 2.2-2.5 km^3 Pre-Kameni island inferred from black, glassy andesite lavas found throughout the LBA deposits, but not in the present Santorini edifice (Druitt and Francaviglia, 1992; Karátson et al., 2018).

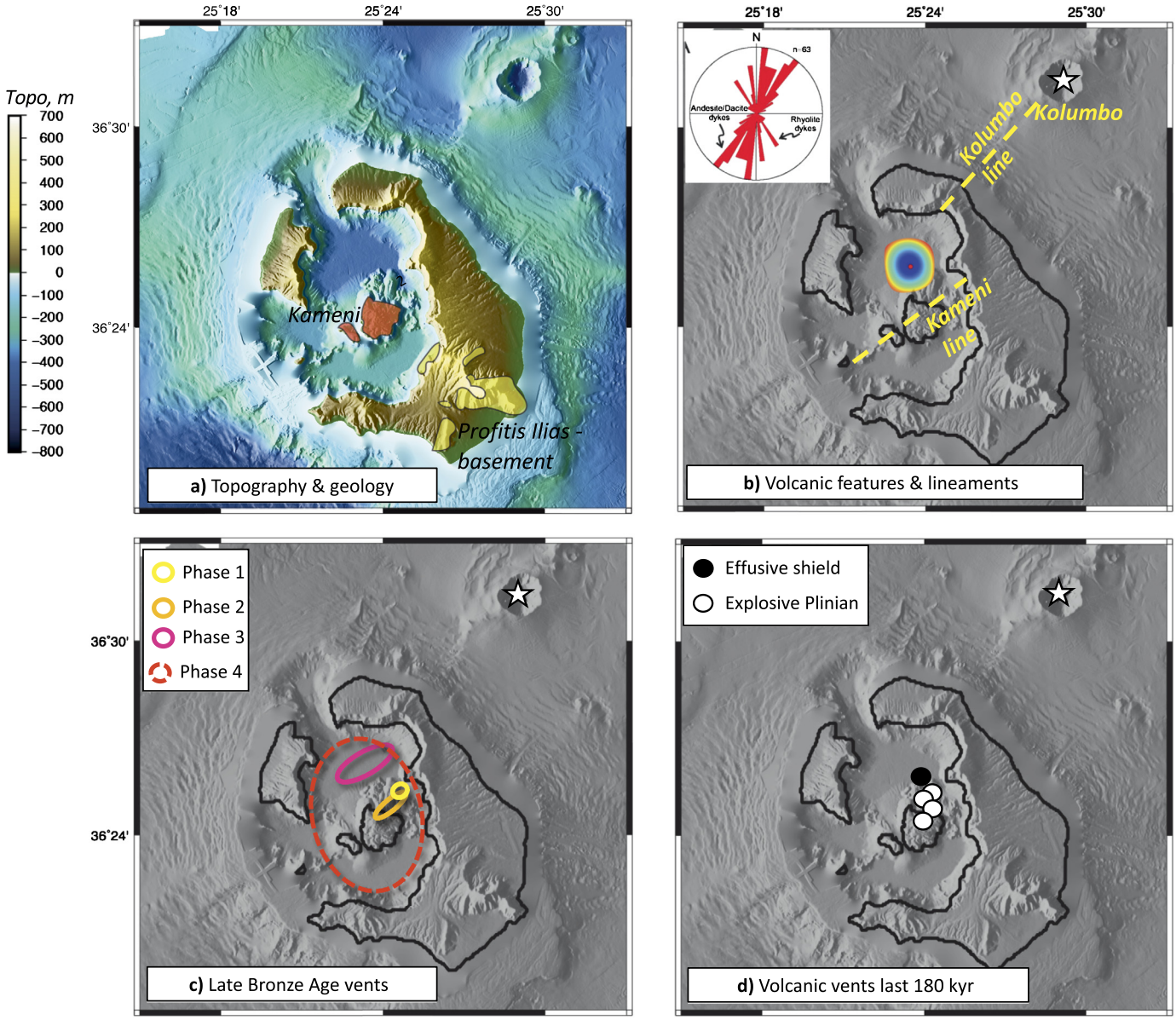

Fig. 2. The geological and volcanic features of Santorini. **(a)** Map of the sea bottom and land topography (Hooft et al., 2017) showing the outcrops of pre-existing basement (yellow) including at the summit of Profitis Ilias and the post-caldera volcanism (red) of the Kameni islands. **(b)** Gray-scale map of topographic gradient showing the Mogi source at 4.5 km depth from GPS-InSAR inversion of 2011-2012 ground deformation (Parks et al., 2015) (red dot is best fit; colors RMS misfit). Volcanic features include Kolumbo seamount (star), the Kolumbo and Kameni lineaments (dashed blue lines). The inset shows dike strikes (Browning et al., 2015) for the Kolumbo lineament. **(c)** Vent locations for the four phases of the Late Bronze Age explosive Plinian eruption. **(d)** Vents for the preceding 180 kyr of explosive Plinian eruptions (white) and effusive caldera-filling shields (black).

Current models for silicic caldera-forming systems involve trans-crustal magmatic systems that evolve significantly over time with rapid final stages of amalgamation preceding the Plinian caldera-forming eruption (Cashman et al., 2017). At Santorini, melt diffusion profiles in orthopyroxene and clinopyroxene crystals from the LBA rhyodacites indicate prolonged storage and segregation of melts in a sub-caldera pluton (8-12 km depth) prior to the LBA eruption (Flaherty, 2018). Since crystals from all eruptive phases yield similar timescales, the authors infer that, on the timescale of a few centuries to years, a shallow (4-6 km) short-lived chamber formed that held most of the magma erupted in the LBA eruption.

The LBA Plinian eruption occurred in 4 geologically distinct main phases (Fig. 2c) with a total eruption volume between 30 and 80 km^3 dense rock equivalent (Bond and Sparks, 1976; Druitt, 2014; Heiken and McCoy, 1984; Johnston et al., 2014; Sparks and Wilson, 1990). The first phase was a Plinian pumice fall indicative of a subaerial eruption. Isopachs of the pumice deposit and the size-distribution of ejected lithics locate the vent on the Pre-Kameni island 1-2 km west of the modern town of Thira (Bond and Sparks, 1976; Druitt and Francaviglia, 1992; Heiken and McCoy, 1984). The second phase is composed of stratified phreatomagmatic base-surges and Plinian deposits showing that variable magma-water interactions occurred at this time (Bond and Sparks, 1976). A higher concentration of lithic blocks in SE Santorini suggests that the vent migrated ~2 km to the SW along a fissure and into the shallow caldera (Heiken and McCoy, 1984; Pfeiffer, 2001).

The third phase of the LBA eruption is a massive, weakly stratified, phreatomagmatic ignimbrite. The gradation from well-stratified surge deposits to massive ash-flow deposits (Bond and Sparks, 1976) and low emplacement temperatures (0 to >250 °C) inferred from paleomagnetic data (McClelland et al., 1990) reflect

increasing water-magma ratios. Deposition of the low-mobility, wet pyroclastic flows beyond the caldera rim suggest that during phase 3 a large tuff-ring (Bond and Sparks, 1976; Sparks and Wilson, 1990) or a mega-tuff cone grew to fill and overtop the existing caldera (~600 m high) (Johnston et al., 2014). Intense magma-water interactions ejected significant lithics up to 10 m in size (Pfeiffer, 2001) including both lavas and tuffs from the caldera floor and black glassy andesites from the Pre-Kameni island (Druitt, 2014). Most of the Pre-Kameni island is thought to have been ejected as lithics during this phase (Karátson et al., 2018). The presence of stromatolite clasts and distribution of large lithics around the northern part of the caldera (Friedrich et al., 1988) indicate that a large new vent opened in the northern caldera basin (Pfeiffer, 2001; Heiken and McCoy, 1984). Pfeiffer (2001) argues that the existing phase 1 and 2 vents may have widened and remained active during this time (Fig. 2c).

The fourth LBA eruption phase is a voluminous, hot (300-500 °C) pyroclastic flow erupted from multiple vents without interaction with water that deposited massive, fine-grained, non-welded ignimbrites in several fans on the coastal plains and in the surrounding sea (Bond and Sparks, 1976; Druitt et al., 1999; Heiken and McCoy, 1984; Sigurdsson et al., 2006; Sparks and Wilson, 1990). The high lithic content in this ignimbrite is considered unusual (Sparks and Wilson, 1990) and the presence of metamorphic basement clasts, especially in the units that erupted first indicate a deeper fragmentation front (Druitt, 2014). These observations point to caldera formation during this last eruption phase that deepened and expanded the existing caldera but remained isolated from the sea (Druitt, 2014; Heiken and McCoy, 1984).

After the LBA eruption ended the caldera flooded catastrophically when its NW rim breached (Nomikou et al., 2016a). A number of small-volume intra-caldera eruptions in the last 3.4 kyr built the Kameni islands (Nomikou et al., 2014; Pyle and Elliott, 2006) (Fig. 2a). Seismic reflection imaging of intra-caldera fill reveals three units that thicken to fill a depression in the northern caldera basin (Johnston et al., 2015). An upper layer, Unit 1, is on average 20 m thick and consists of modern sediments deposited after the Kameni islands became subaerial. The underlying Unit 2 is about 40-50 m thick and merges with the Kameni volcanics indicating it formed during post-LBA intra-caldera shallow-water phreatomagmatism. Unit 3 is up to 150-200 m thick in the center of the northern caldera basin, and in the southern caldera basin, and is internally faulted. The authors interpret this unit to be downfaulted Minoan pyroclastic deposits that overlie pre-Minoan volcanic basement.

Recently, in 2011-2012, Santorini underwent an episode of unrest that included ground inflation consistent with a Mogi source of volume change ~0.02 km^3 at 4.5 km depth (Parks et al., 2015) and seismic swarms on the Kameni lineament (Konstantinou et al., 2013; Papadimitriou et al., 2015) (Fig. 2b). The Kolumbo and Kameni lineaments are alignments of volcanic vents and dikes within the Santorini edifice inferred to relate to tectonic extensional stresses and/or structures (Druitt et al., 1999) (Fig. 2a) and the Kolumbo line extends from the Santorini volcanic complex toward the nearby Kolumbo seamount (Fig. 2b).

3. Seismic experiment and data

Because Santorini's geological evolution and the latest caldera-forming eruption are well understood it is an ideal target for imaging the magmatic system of an arc volcano. We collected a dense, marine-land active source seismic dataset at Santorini volcano in the November-December of 2015. The PROTEUS experiment recorded ~14,300 controlled-sound sources from the 3600 cubic inch airgun array of the *R/V Marcus Langseth* on 90 ocean-bottom and 65 land seismometers and covered an area of 120 × 60 km^2 centered on Santorini (Fig. 1). Heath et al. (submitted) provides a complete description of the experiment, the seismic data, and the tomographic inversion, which we summarize below.

The travel time dataset includes over 200,000 first arrival times of crustal refractions (Pg) that were picked first automatically and then manually. Data were picked on either the hydrophone, vertical, or a stack of the hydrophone and vertical channels using a causal 4th order Butterworth filter of 5-25 Hz. Tens of thousands of high signal-to-noise arrivals were picked automatically using opendTect (https://www.dgbes.com) and were assigned one-sigma errors of 10 msec. One-sigma errors for the manual picks were visually assigned and ranged from 5 to 30 msec. The data set includes travel time arrivals for shots with ranges up to 65 km, with high quality data between 10-30 km at many stations.

4. Tomographic inversion and results

We obtained a high-resolution seismic image of caldera structure at Santorini using a seismic tomography method to invert first-arriving compressional wave travel times for a P-wave velocity model (Toomey et al., 1994). In this paper we present a 25 km × 25 km × 3 km subset (Figs. 3 and 4) of a seismic velocity model that covers the entire domain of the PROTEUS seismic experiment (Heath et al., submitted).

4.1. Inversion

Heath et al. (submitted) inverted the Pg travel time arrivals using a tomographic method that minimizes the prediction error and penalizes the magnitude and roughness of model perturbations (Toomey et al., 1994). The travel times were calculated using a shortest path algorithm (Moser, 1991). The seismic slowness model was gridded at 200 m and extended 125 km × 45 km × 12 km in the horizontal (x parallel to the shot lines) and vertical directions. The slowness model was sheared vertically to include the bathymetry (Toomey et al., 1994) and water wave travel times to the seafloor were calculated on a 50 m by 50 m elevation grid (water velocity = 1.52 km/s). The perturbational grid for the inverse problem was spaced 400 m × 400 m × 200 m in the horizontal and vertical directions. New forward travel times are calculated after each iteration of the inverse problem (Toomey et al., 1994). Tens of inversions were conducted to determine the most appropriate inversion parameters. The final model used horizontal and vertical smoothing parameters of 200 and 100, respectively, and a penalty of 1 was used for model perturbations relative to the previous model. Each inversion consisted of 5 model iterations. The model presented here (Figs. 3 and 4) was fit to a root mean squared misfit of 15 msec, which corresponds to a χ^2 of 2.2.

4.2. Synthetic tomography resolution tests

To analyze the resolution of features in the final model we conducted several synthetic tests. First, we superimposed sinusoidal checkerboard anomalies with horizontal wavelengths of 3 km and amplitude ±0.25 km/s on the 1D velocity structure (Fig. S1). For the 1.6 and 2.8 km depth slices, the checkers had vertical wavelengths of 1 km and were centered at 1.6 km depth. Checkers were recovered with amplitudes 50-80% of the input values indicating that features of this size are well resolved. We note that the reversal of the sign of the velocity anomaly between 1.6 and 2.8 km depth is well recovered. For the 1.0 km depth slice the checkers had 2 km vertical wavelength and were centered at 1 km depth because the seismic rays average the structure above 1 km; recovery at this depth is 60-80%. Checkers beneath the center of eastern

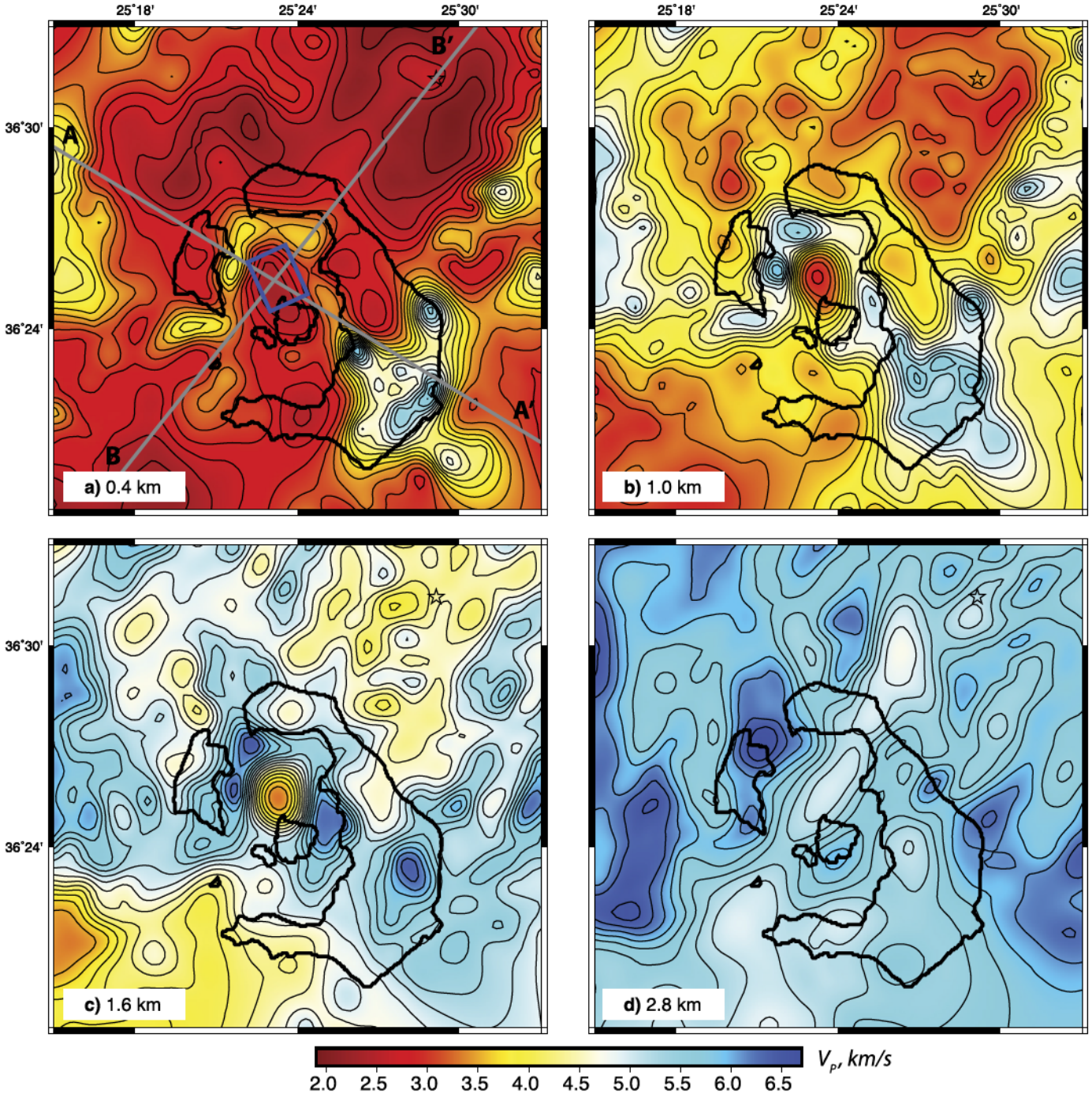

Fig. 3. Maps of P-wave seismic velocity at Santorini. Depth slices through the tomographic model at 400 m (**a**), 1 km (**b**), 1.6 km (**c**) and 2.8 km (**d**) depth below the seafloor. Contour interval is 0.2 km/s. In (**a**) the gray lines show the profiles A-A′ and B-B′ in Fig. 4 and the blue rectangle the area that was averaged to obtain the velocity-depth curve for the caldera profile in Fig. 5a. Note the cylindrical low velocity anomaly in the upper 3 km beneath the north-central caldera with the most pronounced velocity reduction between 1 and 2 km depth.

Santorini are not well recovered because of poor coupling of the island seismometers in the LBA ignimbrite deposits. Checkers south of Santorini are not well recovered because the seismic experiment did not sample this area.

In the second synthetic test, we superimposed a cylinder with a 1 km/s velocity reduction at the location of the observed caldera low-velocity anomaly (Fig S2). The cylinder had diameter 3 km and height 4 km. Recovery is good down to about 3 km depth below which the recovered amplitude decreases. The width of the anomaly is reduced because the spatial smoothing constraint cannot capture the abrupt velocity change imposed in the synthetic model. Both resolution tests show that the magnitude of velocity anomalies will be under recovered in the tomographic inversion.

4.3. Tomography results

The seismic velocity structure of the uppermost crust at Santorini (Figs. 3 and 4) reveals a pronounced vertical cylinder of anomalously low velocities within the north basin of the caldera. Low velocities fill most of the upper ~400 m of the topographic

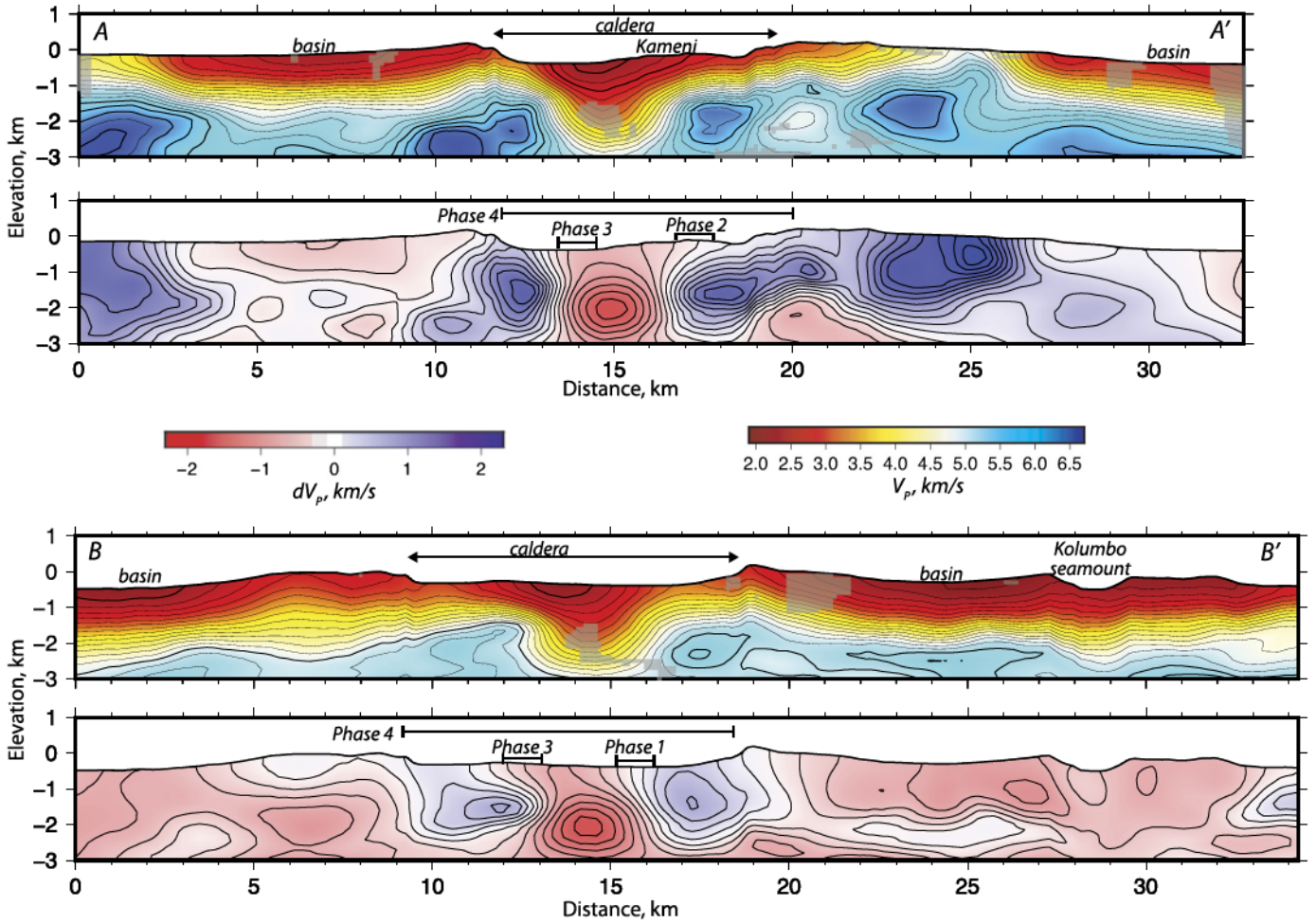

Fig. 4. Cross-sections of seismic velocity along profile A-A′ and B-B′. P-wave velocity and P-wave velocity anomalies relative to the velocity-depth structure of the Anydros metamorphic block (Fig. 5a) along a NW-SE and a SW-NE profile. Contour interval is 0.2 km/s. Low velocities near the seafloor delineate sedimentary basins on the flanks of the volcano. The deeper low-velocity anomaly at 1-2 km depth north of the Kameni islands spatially correlates with the first three phases of the LBA eruption. The topographic caldera corresponds with phase 4 of the LBA eruption. Higher velocities are inferred to be due to metamorphic and/or plutonic rocks.

caldera and their distribution reflects that of the intra-caldera fill imaged using seismic reflection (Johnston et al., 2015) (Fig. 3a and Fig. S3). The anomalous low-velocity cylinder lies below this (between 0.5 and 3 km depth) and is narrowly confined compared to the topographic caldera (diameters of 3 km and 10 km, respectively). It is located north of the Kameni islands and lies between the Kolumbo and Kameni lineaments (Fig. 2b). The low-velocity anomaly extends down to 3 km depth, has a 3.0 ± 0.5 km diameter and, between 1 and 2 km depth, has a substantial velocity reduction of >2 km/s (V_P ~3.2 km/s) compared to the surroundings (Fig. 4). The velocity-depth gradient below 1 km differs from that of the surrounding metamorphic horsts (Fig. 5a); velocities increase very slowly between 1 and 2 km depth, more rapidly from 2 to 2.5 km depth, followed by another gradual increase between 2.5 and 3 km depth (V_P ~5.0 ± 0.1 km/s). The low-velocity cylinder is unusual because it underlies only a portion of the caldera floor and has a significant reduction in velocity.

The low-velocity cylinder is surrounded by high-velocity rocks (V_P of 5.7-6.5 km/s) (Fig. 3). At depths less than 2.5 km, the high velocity regions are arc-shaped and contained within the northwest and southeast parts of the topographic caldera – a geometry indicative of solidified intrusives. At deeper depths high velocities extend beyond the caldera and are aligned NE, similar to the orientation of regional horsts of extended basement (Figs. 1 and 3d). High velocities beneath southeast Santorini (5.5 km/s at 0.4 and 1 km depth) are located where metamorphic basement rocks outcrop at the surface (Figs. 2a and 3a and b). Grabens between the associated horsts coincide with low-velocity sedimentary basins (Nomikou et al., 2016b; Piper and Perissoratis, 2003; Tsampouraki-Kraounaki and Sakellariou, 2018) northeast and southwest of the volcano (Fig. 3a and b). On the basis of these correlations, we infer that the anomalously high velocities are due to plutonic and metamorphic rocks.

5. Calculation of physical properties

To understand the subsurface structure of the Santorini caldera we infer physical properties from seismic velocity. Seismic velocities are controlled by various physical properties including composition, temperature, pressure, porosity, and the nature of the pore-filling material. We argue below that the observed low-V_P anomaly between 1 and 2 km depth in the north central caldera is caused by increased porosity filled with hot seawater (Fig. 5) and that the alternative where melt fills the pore spaces is unlikely.

We estimate the porosity required to explain the observed V_P in the north central caldera by comparing the V_P profile in the caldera to a reference V_P profile for the basement (Fig. 5a and c). We first apply pressure and temperature corrections (Text S1). While we take care to choose appropriate geotherms for the temperature correction, the calculated porosities are far more sensitive to uncertainties in the pore aspect ratio than to uncertainties in the thermal structure (Fig. 5). The reference metamorphic profile

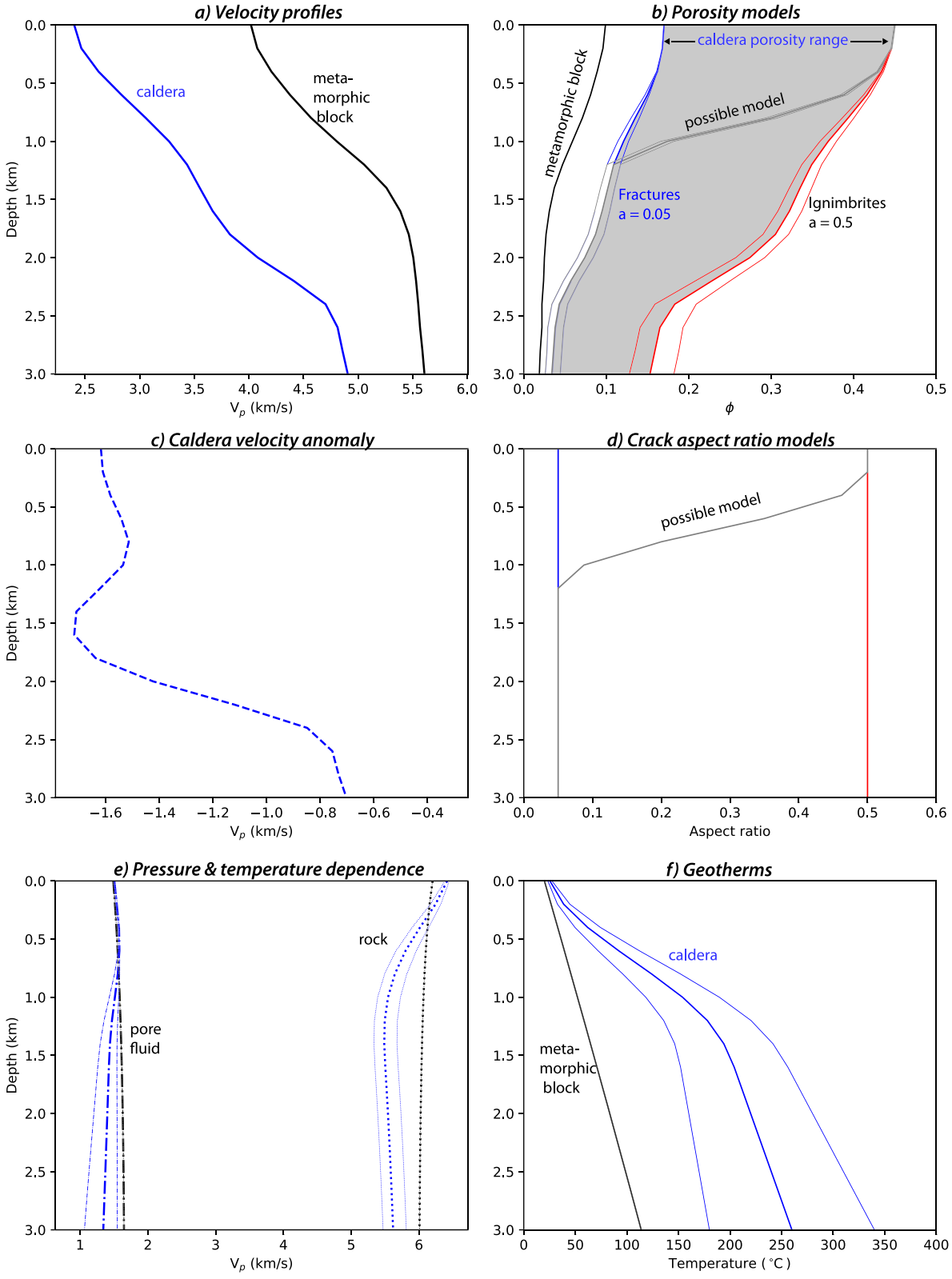

Fig. 5. Predicted porosity for the northern caldera low-velocity anomaly and the reference metamorphic profile. **(a)** The velocity-depth structure of the caldera (blue) and the reference metamorphic profiles (black) obtained by averaging the velocity model over the blue and black rectangles in Figs. 3 and 1, respectively. **(c)** The caldera velocity anomaly (dashed blue) is the difference between the caldera and reference metamorphic profiles in **(a)**. **(b)** The porosity-depth structure is predicted for the reference profile (black) using a pore aspect ratio of 0.05 corresponding to cracks. The range of caldera porosity structures (gray field) corresponds to end-member pore aspect ratios from 0.5 (red) to 0.05 (blue) **(d)**. A geologically motivated model where pore aspect ratio decreases with depth (gray) is also shown in **(b)** and **(d)**. **(e)** A correction to the predicted rock (dotted) and pore fluid (dot-dashed) velocities was applied for pressure and temperature effects of hot caldera (blue) and cooler reference (black) geotherms. **(f)** For the metamorphic profile we use 40 °C/km for a volcanic back arc. The caldera geotherm is not well known and gradients that varied by ±40 °C/km (thin blue), and their corresponding effect on pore fluid and rock velocity, and on predicted porosity, are shown in **(e)** and **(b)**, respectively. See Text S1 for details.

is generated using a rock of schists and limestones with $V_P = 6.5$ km/s (Christensen and Stanley, 2003) and a background geotherm of 40 °C/km. In the caldera, we use a granitic rock with $V_P = 6.2$ km/s (Christensen and Stanley, 2003) and a hotter geotherm estimated from measurements at Santorini and Milos. For the caldera geotherm, the pore fluid we model consists of hot seawater since the temperature remains below 370 °C.

To estimate water-filled porosity we use a self-consistent effective medium approach that treats fluid inclusions as randomly oriented interconnected spheroids (Berryman, 1980). More recent treatments include anisotropy (e.g., Mainprice, 1997) or specific inclusion geometries (Jakobsen et al., 2000; e.g., Taylor and Singh, 2002) and are more complicated than warranted by our lack of knowledge of the subsurface microstructures. The elastic properties of the pore fluid are calculated for the temperature and pressure of each profile (Fig. 5e). For the metamorphic reference profile, we assume that the porosity is in the form of cracks with a pore aspect ratio of 0.05 and we obtain a porosity that decreases from 10% at the surface to 2% at 3 km depth (porosities between 1 and 2 km depth decrease from 7% to 3%) (Fig. 5b).

For the caldera profile, we consider two end-members for the porosity structure of the low-velocity anomaly (Fig. 5b and d). In the first case, we assume it consists of tuffs and ignimbrites with a pore aspect ratio of 0.5. This model is an upper bound for the porosity because of the low sensitivity of seismic velocity to relatively equant inclusions. We obtain a porosity of 37% to 27% between 1 and 2 km depth, which is an anomalous porosity relative to the reference profile of 30% to 24%. In the second case, we assume that the low-velocity anomaly is due to fractured igneous rocks with a pore aspect ratio of 0.05. This model provides a lower bound on the porosity because seismic velocity is very sensitive to crack-shaped inclusions. The resulting porosity is 12% to 7% between 1 and 2 km depth – an anomalous porosity relative to the reference profile of 5% to 4%. Using these two end members as bounds, the average anomalous porosity between 1 and 2 km depth ranges from 4 to 28% (Fig. 5b).

A third geologically motivated structure might have pore aspect ratios that change with depth. One example is labeled 'possible model' in Fig. 5b and d and has ignimbrites and tuffs with aspect ratio 0.5 in the upper 750 m transitioning to fractured rocks with aspect ratio 0.05 beneath. The upper layer represents a ∼150-m-thick layer of post-LBA deposits overlying a layer of ignimbrites and tuffs that is 200 to 600 m thick on the basis of seismic reflection imaging and geological models (Johnston et al., 2015, 2014). In this upper layer porosities are large, 45%, and the predicted porosity decreases rapidly at the depth where the pore aspect ratio becomes smaller. The unknown subsurface geology makes a range of models with depth-varying pore aspect ratios possible that would lie within the gray field in Fig. 5b. More accurate constraints on the physical properties and pore geometries can be obtained from joint analysis with shear waves (in particular Vp/Vs ratios), gravity modeling, and drilling within the caldera.

Although our preferred interpretation of the low-velocity volume at 1.5 km depth is water porosity at high temperature, a rhyolite or andesite partial melt could also explain the low V_P. In this scenario we would attribute the V_P anomaly to thermal effects up to the solidus and any further reduction of seismic velocity to melt using the same approach as above (Fig. S4). We isolate the portion of the V_P anomaly in the caldera that cannot be explained simply with increased temperatures up to the solidus of andesite (800 °C). For the pore fluid, we use elastic properties for a silicic partial melt with a bulk modulus of 2.2 GPa and a density of 2300 kg/m^3. For melt, we chose pore aspect ratio end-members of 0.05 and 0.2 for grain boundary and triple-junction geometries, respectively. This interpretation predicts melt fractions ranging from 13% to 26% at 1.5 km depth. For average porosities of 10% to 22% between 1 and 2 km depth, this implies 0.5 to 2.2 km^3 of melt assuming a vertical cylindrical volume.

While some petrologic and geophysical studies have suggested shallow melt ponding at Santorini (Cottrell et al., 1999; Druitt et al., 2016; Saltogianni et al., 2014), we consider that a large volume of melt at shallow depths is inconsistent with most geological and geophysical observations of the current magmatic system. These observations include that: magma ponding depths of 4-6 km are inferred from melt inclusion saturation pressures for 726 AD Kameni lavas (Druitt, 2014); earthquakes extended to at least 5 km depth during the recent unrest period (Konstantinou et al., 2013; Papadimitriou et al., 2015); and fluxes of magmatic gases and hydrothermal heat within the caldera are relatively low (Papadimitriou et al., 2015; Parks et al., 2013). Consequently, we infer the low-velocity anomaly beneath the north central caldera is caused by a vertical cylindrical volume with a porosity that, between 1 and 2 km depth, is 4-28% higher than the local reference and is filled with high temperature water. This region is likely to be the main hydrothermal reservoir of Santorini (Tassi et al., 2013) and the potential for interaction between rising magma and water in the imaged high-porosity volume is a geo-hazard that needs to be further assessed.

6. Discussion

The discovery of an anomalous low-velocity, high-porosity vertical cylinder extending from 0.5 to 3 km depth, that is confined to the north central caldera (Figs. 3 and 4), is new and was not predicted by existing studies at Santorini. The seismic tomography and reflection data reveal: (i) an inner cylinder of high porosity down to 3 km depth, and (ii) more coherent, down-faulted strata with a maximum thickness of 200 m above the inner cylinder (Johnston et al., 2015).

Geological reconstructions of the pre-LBA caldera and its volcanic stratigraphy provide a starting structure that was modified during the LBA eruption and caldera formation (Fig. 6a). This includes the remnants of the Skaros-Thirasia lava shields and their hyaloclastite cores that collapsed during the Cape Riva eruption to form the shallow pre-LBA caldera (Sparks and Wilson, 1990). We estimate a thickness of 400-600 m on the basis of the inferred 350-m elevation of the Skaros lava shield summit (Druitt et al., 1999; Heiken and McCoy, 1984). After the Cape Riva eruption and prior to the LBA eruption the Pre-Kameni island was built of black, glassy andesites and may also have had a hyaloclastite core. Most of the Pre-Kameni island is thought to have been ejected as lithics during the LBA eruption (Karátson et al., 2018). The primary low-velocity anomaly recovered in this study lies at 1-2 km depth and is located below these pre-existing deposits (Fig. 6a).

The imaged low-velocity anomaly also lies between the Kolumbo and Kameni lineaments (KL2 and KL1, respectively in Fig. 6a). These volcanic alignments appear to be long-lived since numerous dikes lie parallel to the down-dropped graben of the Kolumbo line (Browning et al., 2015) and since earlier volcanic vents, both for intra-caldera effusive and Plinian explosive eruptions, lie near the Kameni line (Fig. 2 a and b). These correlations suggest that the low-density column may have existed prior to the LBA event and be long-lived; to reflect this uncertainty we show it with a question mark in Fig. 6a.

The observed seismic velocity structure correlates with the four phases of the LBA eruption as follows. The initial phase 1 and phase 2 vents (Druitt, 2014; Heiken and McCoy, 1984; Pfeiffer, 2001) are associated with the southeast boundary of the low-velocity cylinder (Fig. 2c). The phase 3 vent is reconstructed within the shallow-water north caldera basin (Heiken and McCoy, 1984; Pfeiffer, 2001) approximately along the northern margin of the low-velocity cylinder (Fig. 2c). Geological observations of several

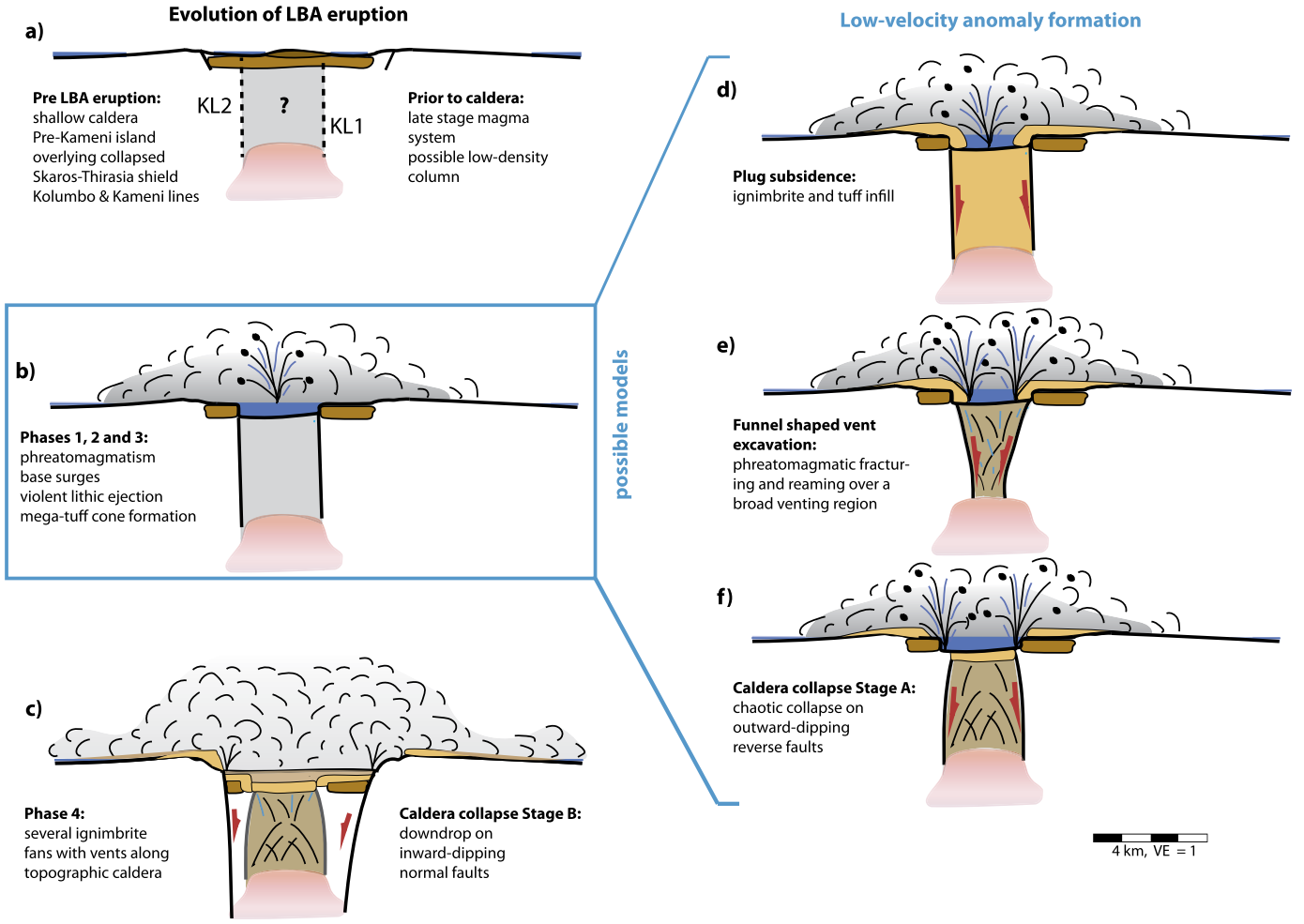

Fig. 6. Conceptual model for the evolution of the LBA eruption and formation of the low-velocity anomaly. **(a)** Prior to the LBA eruption the Pre-Kameni island is located within a shallow caldera that overlies the collapsed Skaros-Thirasia shields with their hyaloclastite cores. The Kameni and Kolumbo lines (KL1 and KL2, respectively) exist and the magmatic system (pink) is in a late stage of evolution. There may be a low-density column (gray) between KL2 and KL1. **(b)** The inner cylindrical low-velocity anomaly is spatially associated with phases 1, 2 and 3 of the LBA eruption that start Plinian and evolve to increasing magma-water interactions with violent lithic ejection and tuff formation. **(c)** Collapse of the topographic caldera and ignimbrite formation occurs during phase 4 of the LBA eruption. We infer the topographic caldera forms by down-drop along inward-dipping normal faults potentially when accessing the deeper part of the magmatic system. Three possible models to form the inner low-velocity anomaly during phases 1 to 3 of the eruption are: **(d)** Subsidence of pre-existing caldera fill and infill with ignimbrites and tuffs; **(e)** Excavation by phreatomagmatic fracturing and reaming over a broad funnel-shaped venting region; **(f)** Inner caldera collapse along outward-dipping reverse faults that fracture the pre-existing caldera fill.

ignimbrite fans distributed around the caldera (Bond and Sparks, 1976; Druitt, 2014; Heiken and McCoy, 1984) and a diverse lithology of ejected rock debris (Druitt and Francaviglia, 1992) indicate that the entire topographic caldera subsided during phase 4 and we observe high velocities beneath the remainder of the caldera floor (Fig. 3a-c). We argue that this last observation implies that the formation of the topographic caldera occurred by coherent down-drop of the larger caldera during the last phase of the LBA eruption (Fig. 6c).

Below we explore three possible end-member models for the formation of the inner seismic low-velocity anomaly (Fig. 6b, d-f); the first two are motivated by the geological observations of the LBA eruption of Santorini, while the third is a general sequence for caldera formation.

6.1. Collapsed plug filled with volcanic deposits

In the first scenario, the low-velocity cylinder is filled with tuffs and ignimbrite products (Fig. 6d) and the average porosity between 1 and 2 km depth is high, ~32%. This interpretation requires extensive foundering of the low-velocity plug and infilling with eruptive products and is similar to that proposed for the larger Valles caldera (Lipman, 1997). Foundering and filling of this space may have happened entirely during the LBA eruption, in which case pre-existing rock 3 km wide and at least 2 km deep (a cylindrical volume of 14 km^3) subsided into the collapsing magmatic system – an interpretation that is compatible with the volume erupted during LBA phases 1 to 3 (14 to 20 km^3 dense rock equivalent excluding the lithics (Karátson et al., 2018)). The correlation of the Kolumbo and Kameni lineaments with the margins of the low-velocity plug, suggests that these structural weaknesses could have facilitated large-scale foundering of the region between them, accompanied by deposition of phreatomagmatic and pyroclastic products in the generated space. The inference that a tuff ring or mega-tuff cone ~600 m tall grew within the caldera during phase 3 of the LBA eruption (Johnston et al., 2014) implies that the plug may have dropped at the end of phase 3 with a majority of the tuff products collapsing into it – in which case the stratigraphic layering observed in Unit 3 of the seismic reflection images of the LBA deposits within the caldera (Johnston et al., 2015) would correspond to overlying phase 4 ignimbrites.

Alternatively, the spatial association of earlier volcanic vents (Druitt et al., 1999) with the low-velocity cylinder, suggests that a tuff/ignimbrite-filled plug may have formed by repeated founder-

ing and infilling of the same region over multiple eruptive cycles at Santorini. This interpretation is consistent with the apparent longevity of the Kolumbo and Kameni lines. In this case, a lesser degree of foundering is needed during the LBA eruption and the structure is built up gradually. A further implication is that the margins of this pre-existing structure then provided pathways for, and localized, LBA vent formation during phases 1 through 3.

6.2. Phreatomagmatic rock breakup

Another possibility is that the high-porosity cylinder formed by rock breakup during the intensely phreatomagmatic phase 3 of the LBA eruption making a large diatreme-like structure (Fig. 6e) (Escher, 1929; Sparks and Wilson, 1990). In this scenario, porosity is dominated by fractures and an average porosity of 9% between 1 and 2 km depth is inferred. Reaming and rock excavation undoubtedly took place given the energy required to eject up to 10-m-diameter lithics during phase 3 (Pfeiffer, 2001). The diatreme may also be the origin of the large tuff-ring proposed to explain deposition of phase 3 flows on the caldera rim (Sparks and Wilson, 1990). While analogue models of diatremes show that the ejected lithics are usually sourced from only a few 100 meters below the surface, it is possible that rock breakup from the powerful phreatomagmatic explosions as well as water penetration contributed to fracturing as deep as 2 km (Valentine et al., 2014). We consider this scenario less likely because the observed seismic anomaly (3 km wide at 1.5 km depth) is larger in spatial extent and depth than the largest studied diatremes, which are 2 km wide and 2 km deep and narrow with depth (White and Ross, 2011).

However, this scenario has features that fit both the geology and the subsurface structure and more study is needed to investigate energy partitioning during large phreatomagmatic eruptions. For example, it is not clear how energy is divided between launching of material and sound waves into the atmosphere versus the passage of shock waves within the underlying rock, hence the spatial extent of hydrofracturing or damage is poorly constrained. Numerical simulations of rock damage by underground explosions suggest that damage extends well away from the cavity (e.g., Johnson and Sammis, 2001) and is more extensive below than above the explosion site (Ma et al., 2011). In addition, post-explosion well-logging studies reveal that explosions that are high in gaseous products or within water-filled media generate more extensive macro-fractures (Stroujkova, 2018). Furthermore, studies of the mechanisms of deep-sea explosive eruptions show that, because the super-critical behavior of seawater is significantly different from that of fresh water, a vapor phase exists at super-critical pressures that is hydrodynamically unstable and results in explosive behavior at high pressures if the magma-water ratios and mixing mechanisms are right (Wohletz, 2003). Further understanding requires modeling of the accumulated damage pattern from repeated phreatomagmatic explosions and their spatial and depth extent given the inferred vent geometry and the fragmentation depth of phase 2 and 3 erupted products.

6.3. Multistage, nested caldera collapse

Our final scenario seeks to put the formation of both the intra-caldera, cylindrical, low-velocity region and the topographic caldera in a framework of evolving caldera deformation as magma continues to be withdrawn over the course of an eruption. In stage A of this scenario, chaotic collapse of the area between the phase 1, 2 and 3 vents occurred forming the high-porosity cylinder in the northern caldera (Fig. 6f). We again speculate that either the vents formed along the Kolumbo and Kameni lines, and consequently the area between them collapsed, or that the cylindrical structure already existed and the LBA vents again formed along its boundaries during collapse (Fig. 6f). Analogue studies show that instabilities during down drop of a 3D plug can cause vent location and eruptive products to vary dramatically during subsidence (Kennedy et al., 2008), potentially explaining the temporal migration of vent locations during phases 1 through 3 and the variations in eruptive products during individual eruptive phases.

In the generalized caldera collapse models, the inner stage A involves breakup of the volume overlying the evacuating magma system by a number of reverse faults propagating upward (Fig. 6f) (Roche et al., 2000; Scandone, 1990; Scandone and Acocella, 2007). If the volume between 1 and 2 km depth is dominated by fractured rock, the porosity is ∼10%. If larger collapse blocks contribute more equant fractures the required porosity would be higher (Fig. 5). Phase 4 ignimbrites likely fill the upper portion of the low-velocity collapse cylinder (Johnston et al., 2015) and the inferred porosity for a model where aspect ratio decreases with depth is illustrated in Fig. 5. Alternatively, porosity may be higher from 1 to 2 km depth because of more intense brecciation below a transverse arch that develops within the collapsing column and acts to support the overlying material (Holohan et al., 2015; Scandone, 1990) (Fig. 6f).

In stage B of this caldera formation scenario, the observation of high velocities beneath the remainder of the caldera (Figs. 3 and 4) suggests that coherent subsidence of the entire topographic caldera to ∼500 m below sea level occurred during phase 4 of the eruption (Figs. 6c). Resolved high velocities within the broader caldera could reflect down-dropped Skaros-Thirasia shield lavas in the upper 500 m and/or igneous rocks along the caldera edges (Sakellariou et al., 2012).

In this scenario, the seismic and geological results from Santorini provide observational evidence for models of multistage, nested caldera formation during progressive caldera subsidence (Acocella, 2006). During stage A, the inner collapse column would be formed along outward-dipping reverse faults with breakup of the roof rock (Fig. 6g). During stage B, a new outer ring of collapse would cause subsidence of the entire topographic caldera and the opening of new vents during phase 4 (Fig. 6d). Accordingly, the geologically distinctive LBA eruptive phases form as a direct result of geological processes occurring during each stage of caldera formation (Fig. 6).

It is quite possible that all three of the above scenarios (Fig. 6e-g) play a role in generating the inner cylinder of high porosities at Santorini. Thus, rock breakup by reverse faulting during inner caldera collapse may be accompanied by, or even promoted by, fracturing and reaming of the volcanic vent during violent magma-water interactions. In addition, the upper portions of the high-porosity cylinder are probably formed by the deposition of eruptive volcanic products including tuffs, pyroclasts, and ignimbrites.

6.4. Present day magma recharge

The spatial correlation of post-collapse volcanism with the upper-crustal low-velocity volume suggests that present-day accumulation of magma in the upper ∼5 km of the crust may be focused beneath the low-density column due to edifice stresses generated by both the low-density cylinder and the caldera topography (Fig. 7). Since the 2011-2012 magmatic inflation episode (Parks et al., 2015) occurred directly beneath the low-velocity cylinder (Fig. 2b), we suggest that a low-density cylinder within the caldera affects the dynamics of the underlying magmatic system. Previous authors have demonstrated that magma emplacement in the upper crust is influenced by stresses within the volcanic edifice due to topographic loads (Corbi et al., 2015; Muller et

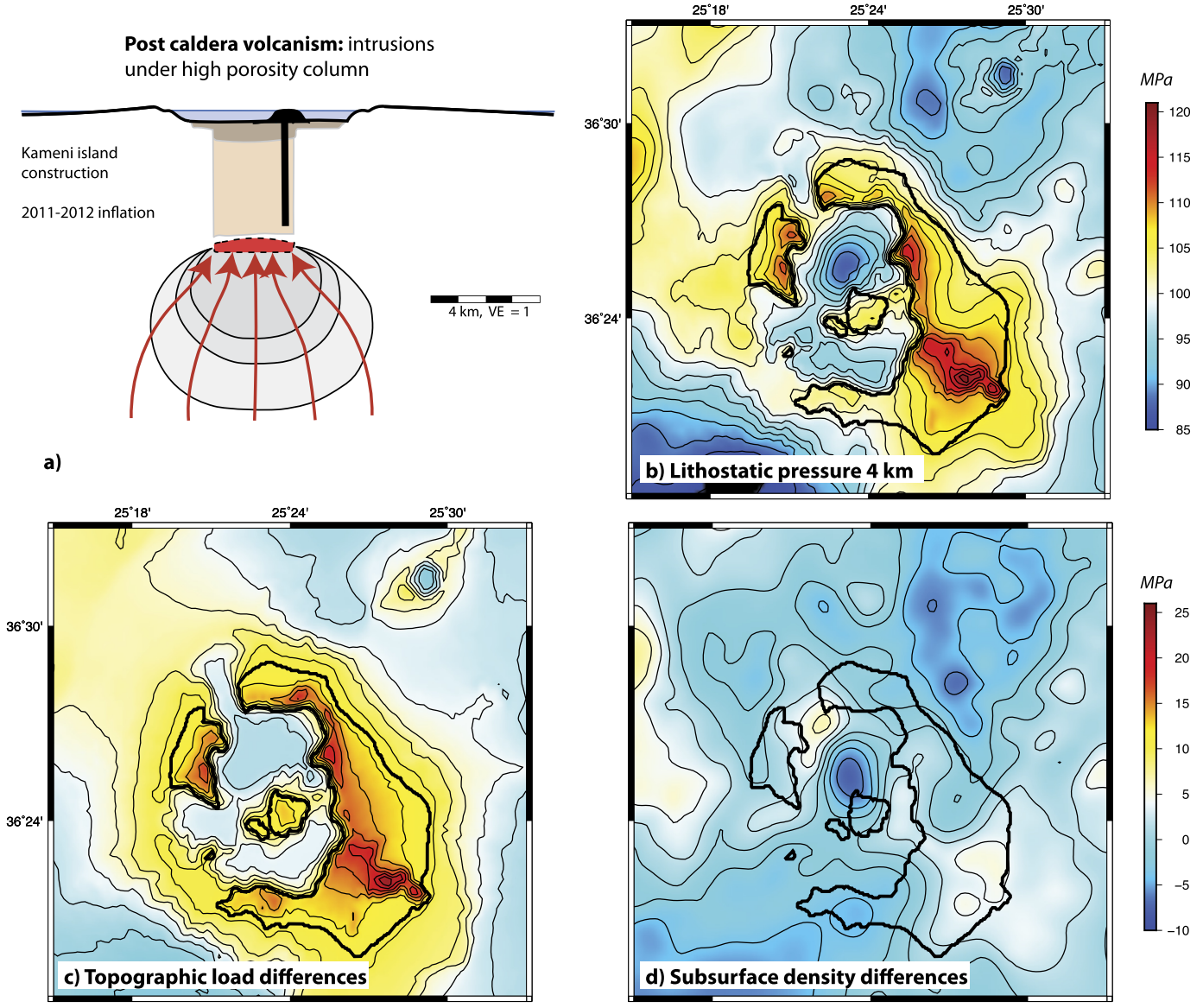

Fig. 7. Comparison of the low-velocity anomaly with magma recharge and predicted lithostatic pressure at 4 km depth. **(a)** Conceptual model where unloading by the low-density column favors intrusion, such as the 2011-2012 inflation, beneath the low-density column. A simple lithostatic calculation suggests that spatial variations in unloading due to density variations in the upper crust are of similar magnitude to those due to unloading by the topography of the volcano. **(b)** Total lithostatic pressure calculated from the seismic velocity model at 4 km depth. The variations in gravitational load due the topography and the water column **(c)** are roughly equal to those from seismically-inferred crustal density variations **(d)**. Contour interval is 2 MPa.

al., 2001; Pinel et al., 2017) and internal structure (Gudmundsson, 1990; Karlstrom et al., 2009). Finite element calculations of edifice stress (Corbi et al., 2015) also show that volcano unloading caused by the topographic depression associated with caldera formation favors sill emplacement beneath the caldera floor because the least compressive stress becomes vertical. A low-density cylinder would unload the volcano in a similar way to caldera formation.

The relative importance of unloading by a low-density anomaly compared to that by caldera formation can be estimated from the lithostatic pressure at 4 km below sea level (Fig. 7). We sum the contributions of the topography, the water column, and the crustal density calculated from seismic velocity using the relationships of Brocher (2005) at each grid point (Fig. 7b-d). The predicted total lithostatic pressure varies from 85 to 120 MPa (Fig. 7b) and has a minimum coincident with the seismic low-velocity anomaly. The topography of the volcanic edifice and the surrounding sea contribute variations of ∼20 MPa to gravitational loading with a broad minimum throughout the caldera except beneath the Kameni islands (Fig. 7c). The calculated differences in gravitational load due to density variations within the upper crust are ∼14 MPa and have a pronounced low beneath the low-velocity anomaly (Fig. 7d). While complete exploration of this idea requires modeling of edifice stresses, gravitational loading from internal density variations is likely to be important since the magnitude is comparable to that from topography (Fig. 7c and d). The correlation of older volcanic vents with the low-velocity anomaly further suggests that a feedback between the internal structure of the volcanic edifice and localization of magma emplacement in the upper crust may have occurred through several eruptive cycles at Santorini. Such a feedback would result in long-lived and actively, self-organized, centralized magmatic activity.

7. Conclusions

To understand caldera formation mechanisms at arc volcanoes we present a P-wave seismic velocity model of the upper crust

at Santorini in the Hellenic volcanic arc of Greece. We find a low-velocity anomaly in the upper 3 km with diameter of 3 ± 0.5 km that is confined beneath the north-central portion of the caldera. We infer that this represents a volume of excess porosity of 4 to 28% filled with hot seawater and argue that the alternative explanation of melt filling the pore spaces is unlikely. The Kolumbo and Kameni lineaments bound the margins of the anomaly and the locations of the vents for the first three phases of the Late Bronze Age eruption correlate with the imaged structure.

We combine our results with previous geological studies to infer that collapse of a limited area of the caldera floor resulted in a high-porosity, low-density cylindrical volume, which formed by either chaotic collapse along reverse faults, wholesale subsidence and infilling with tuffs and ignimbrites, phreatomagmatic fracturing, or a combination of these processes. Phase 4 eruptive vents are located along the margins of the topographic caldera and the velocity structure indicates that coherent down-drop of the wider topographic caldera followed more limited collapse in the northern caldera. This progressive collapse sequence is consistent with models for multi-stage formation of nested calderas along conjugate reverse and normal faults. If this model holds, each stage of caldera formation could produce the geologically distinctive eruptive phases of the LBA eruption.

The pressure source of edifice inflation during 2011-2012 unrest lies at ∼4.5 km depth, directly beneath the cylindrical low-density anomaly, and we hypothesize that sub-surface density anomalies influence present-day magma recharge. The correlation of older volcanic vents with the low-velocity anomaly further suggests that this conduit system may be long-lived. We postulate that past collapse mechanisms at Santorini influence magma focusing between eruptive cycles, an actively self-organized feedback process that may be important in other volcanoes.

Author contributions

E.E.E.H. wrote the manuscript with comments from the co-authors and drafted all the figures except Figs. 4 and 5. All authors discussed the results and their implications and assisted in revising the manuscript. B.A.H. performed the data picking and tomographic analysis and drafted Fig. 4; E.E.E.H. and D.R.T. supervised the project. M.P. performed the calculation of physical properties and drafted Fig. 5. E.E.E.H., D.R.T, J.V.M, C.B.P. P.N., and M.W. designed, funded, permitted, and executed the data collection.

Acknowledgements

For their roles in the data collection, we thank the officers, crew, and marine management office of the *R/V Marcus G. Langseth*, the OBS teams from Scripps Institution of Oceanography and Woods Hole Oceanographic Institution and their staff, and the graduate and undergraduate students who participated in both the island and marine deployments. Additional assistance was provided by onboard passive acoustic technicians and marine mammal observers to ensure that the project was in compliance with guidelines set forth by marine environmental assessments and permits. The Greek military provided helicopter support for seismometer installation on the smaller islands. We thank Tim Druitt, Thomas Giachetti, Gene Humphreys, Stephen Sparks, Amanda Thomas, and Josef Dufek for helpful discussions and/or reviews. The experiment and analysis were supported by the National Science Foundation under grant number OCE-1459794 to the University of Oregon and Leverhulme Grant RPG-2015-363 to Imperial College London.

Appendix A. Supplementary material

Supplementary material related to this article can be found online at https://doi.org/10.1016/j.epsl.2019.02.033.

References

Acocella, V., 2006. Caldera types: how end-members relate to evolutionary stages of collapse. Geophys. Res. Lett. 33, L18314. https://doi.org/10.1029/2006GL027434.

Anadón, P., Canet, C., Friedrich, W.L., 2013. Aragonite stromatolitic buildups from Santorini (Aegean Sea, Greece): geochemical and palaeontological constraints of the caldera palaeoenvironment prior to the Minoan eruption (ca 3600 yr bp). Sedimentology 60, 1128–1155. https://doi.org/10.1111/sed.12025.

Aramaki, S., 1984. Formation of the Aira Caldera, southern Kyushu, ∼22,000 years ago. J. Geophys. Res., Solid Earth (1978–2012) 89, 8485–8501. https://doi.org/10.1029/JB089iB10p08485.

Athanassas, C.D., Bourlès, D.L., Braucher, R., Druitt, T.H., Nomikou, P., Léanni, L., 2016. Evidence from cosmic ray exposure (CRE) dating for the existence of a pre-Minoan caldera on Santorini, Greece. Bull. Volcanol. 78, 1–13. https://doi.org/10.1007/s00445-016-1026-3.

Beachly, M.W., Hooft, E.E.E., Toomey, D.R., Waite, G.P., 2012. Upper crustal structure of Newberry Volcano from P-wave tomography and finite difference waveform modeling. J. Geophys. Res. 117, B10311. https://doi.org/10.1029/2012JB009458.

Berryman, J.G., 1980. Long-wavelength propagation in composite elastic media I. Spherical inclusions. J. Acoust. Soc. Am. 68, 1809–1819. https://doi.org/10.1121/1.385172.

Bond, A., Sparks, R.S.J., 1976. The Minoan eruption of Santorini, Greece. J. Geol. Soc. 132, 1–16. https://doi.org/10.1144/gsjgs.132.1.0001.

Brocher, T.M., 2005. Empirical relations between elastic wavespeeds and density in the Earth's crust. Bull. Seismol. Soc. Am. 95, 2081–2092. https://doi.org/10.1785/0120050077.

Browning, J., Drymoni, K., Gudmundsson, A., 2015. Forecasting magma-chamber rupture at Santorini volcano, Greece. Sci. Rep. 5, 15785. https://doi.org/10.1038/srep15785.

Cashman, K.V., Sparks, R.S.J., Blundy, J.D., 2017. Vertically extensive and unstable magmatic systems: a unified view of igneous processes. Science 355, eaag3055. https://doi.org/10.1126/science.aag3055.

Christensen, N.I., Stanley, D., 2003. Seismic velocities and densities of rocks. In: International Handbook of Earthquake and Engineering Seismology, vol. 81, pp. 1587–1594.

Corbi, F., Rivalta, E., Pinel, V., Maccaferri, F., Bagnardi, M., Acocella, V., 2015. How caldera collapse shapes the shallow emplacement and transfer of magma in active volcanoes. Earth Planet. Sci. Lett. 431, 287–293. https://doi.org/10.1016/j.epsl.2015.09.028.

Cottrell, E., Gardner, J.E., Rutherford, M.J., 1999. Petrologic and experimental evidence for the movement and heating of the pre-eruptive Minoan rhyodacite (Santorini, Greece). Contrib. Mineral. Petrol. 135, 315–331. https://doi.org/10.1007/s004100050514.

Deplus, C., Bonvalot, S., Dahrin, D., Diament, M., Harjono, H., Dubois, J., 1995. Inner structure of the Krakatau volcanic complex (Indonesia) from gravity and bathymetry data. J. Volcanol. Geotherm. Res. 64, 23–52. https://doi.org/10.1016/0377-0273(94)00038-I.

Druitt, T.H., 2014. New insights into the initiation and venting of the Bronze-Age eruption of Santorini (Greece), from component analysis. Bull. Volcanol. 76, 794. https://doi.org/10.1007/s00445-014-0794-x.

Druitt, T.H., Edwards, L., Mellors, R.M., Pyle, D.M., Sparks, R.S.J., Lanphere, M., Davies, M., Barreiro, B., 1999. Santorini volcano. Mem. Geol. Soc. Lond. 19, 165 pp.

Druitt, T.H., Francaviglia, V., 1992. Caldera formation on Santorini and the physiography of the islands in the late Bronze Age. Bull. Volcanol. 54, 484–493. https://doi.org/10.1007/BF00301394.

Druitt, T.H., Mercier, M., Florentin, L., Deloule, E., Cluzel, N., Flaherty, T., Médard, E., Cadoux, A., 2016. Magma storage and extraction associated with Plinian and Interplinian activity at Santorini caldera (Greece). J. Petrol. 57, 461–494. https://doi.org/10.1093/petrology/egw015.

Escher, B.G., 1929. On the formation of calderas. Leidsche Geolog. Mededeling. 3, 183–219.

Fabbro, G.N., Druitt, T.H., Scaillet, S., 2013. Evolution of the crustal magma plumbing system during the build-up to the 22-ka caldera-forming eruption of Santorini (Greece). Bull. Volcanol. 75, 1–22. https://doi.org/10.1007/s00445-013-0767-5.

Farrell, J., Smith, R.B., Husen, S., Diehl, T., 2015. Tomography from 26 years of seismicity revealing that the spatial extent of the Yellowstone crustal magma reservoir extends well beyond the Yellowstone caldera. Geophys. Res. Lett. 41, 3068–3073. https://doi.org/10.1002/(ISSN)1944-8007.

Flaherty, T., 2018. Multiple timescale constraints for high-flux magma chamber assembly prior to the Late Bronze Age eruption of Santorini (Greece). Contrib. Mineral. Petrol. 173, 75. https://doi.org/10.1007/s00410-018-1490-1.

Friedrich, W.L., Eriksen, U., Tauber, H., Heinemeier, J., Rud, N., Thomsen, M.S., Buchardt, B., 1988. Existence of a water-filled caldera prior to the Minoan eruption of Santorini, Greece. Naturwissenschaften 75, 567–569. https://doi.org/10.1007/BF00377720.

Gudmundsson, A., 1990. Emplacement of dikes, sills and crustal magma chambers at divergent plate boundaries. Tectonophysics 176, 257–275. https://doi.org/10.1016/0040-1951(90)90073-H.

Gudmundsson, M.T., Jónsdóttir, K., Hooper, A., Holohan, E.P., Halldórsson, S.A., Ófeigsson, B.G., Cesca, S., Vogfjörd, K.S., Sigmundsson, F., Högnadóttir, T., Einarsson, P., Sigmarsson, O., Jarosch, A.H., Jónasson, K., Magnússon, E., Hreinsdóttir, S., Bagnardi, M., Parks, M.M., Hjörleifsdóttir, V., Pálsson, F., Walter, T.R., Schöpfer, M.P.J., Heimann, S., Reynolds, H.I., Dumont, S., Bali, E., Gudfinnsson, G.H., Dahm, T., Roberts, M.J., Hensch, M., Belart, J.M.C., Spaans, K., Jakobsson, S., Gudmundsson, G.B., Fridriksdóttir, H.M., Drouin, V., Dürig, T., Aðalgeirsdóttir, G., Riishuus, M.S., Pedersen, G.B.M., van Boeckel, T., Oddsson, B., Pfeffer, M.A., Barsotti, S., Bergsson, B., Donovan, A., Burton, M.R., Aiuppa, A., 2016. Gradual caldera collapse at Bárdarbunga volcano, Iceland, regulated by lateral magma outflow. Science 353, aaf8988. https://doi.org/10.1126/science.aaf8988.

Heath, B.A., Hooft, E.E.E., Toomey, D.R., Papazachos, C.B., Nomikou, P., Paulatto, M., Morgan, J.V., Warner, M.R., submitted. Tectonism and its relation to magmatism around Santorini volcano from upper crustal P-wave velocity. J. Geophys. Res.

Heath, B.A., Hooft, E.E.E., Toomey, D.R., Bezada, M.J., 2015. Imaging the magmatic system of Newberry Volcano using joint active source and teleseismic tomography. Geochem. Geophys. Geosyst. 16, 4433–4448. https://doi.org/10.1002/2015GC006129.

Heiken, G., McCoy, F., 1984. Caldera development during the Minoan eruption, Thira, Cyclades, Greece. J. Geophys. Res. 89, 8441–8462. https://doi.org/10.1029/JB089iB10p08441.

Holohan, E.P., Schöpfer, M.P.J., Walsh, J.J., 2015. Earth Planet. Sci. Lett. 421, 139–151. https://doi.org/10.1016/j.epsl.2015.03.003.

Hooft, E.E.E., Nomikou, P., Toomey, D.R., Lampridou, D., Getz, C., Christopoulou, M.-E., O'Hara, D., Arnoux, G.M., Bodmer, M., Gray, M., Heath, B.A., VanderBeek, B.P., 2017. Backarc tectonism, volcanism, and mass wasting shape seafloor morphology in the Santorini-Christiana-Amorgos region of the Hellenic Volcanic Arc. Tectonophysics 712–713, 396–414. https://doi.org/10.1016/j.tecto.2017.06.005.

Jakobsen, M., Hudson, J.A., Minshull, T.A., Singh, S.C., 2000. Elastic properties of hydrate-bearing sediments using effective medium theory. J. Geophys. Res. 105, 561–577. https://doi.org/10.1029/1999JB900190.

Johnson, L.R., Sammis, C.G., 2001. Effects of rock damage on seismic waves generated by explosions. Pure Appl. Geophys. 158, 1869–1908. https://doi.org/10.1007/PL00001136.

Johnston, E.N., Sparks, R.S.J., Nomikou, P., Livanos, I., Carey, S., Phillips, J.C., Sigurdsson, H., 2015. Stratigraphic relations of Santorini's intracaldera fill and implications for the rate of post-caldera volcanism. J. Geol. Soc. Lond. 172, 323–335. https://doi.org/10.1144/jgs2013-114.

Johnston, E.N., Sparks, R.S.J., Phillips, J.C., Carey, S., 2014. Revised estimates for the volume of the Late Bronze Age Minoan eruption, Santorini, Greece. J. Geol. Soc. 171, 583–590. https://doi.org/10.1144/jgs2013-113.

Karátson, D., Gertisser, R., Telbisz, T., Vereb, V., Quidelleur, X., Druitt, T., Nomikou, P., Kósik, S., 2018. Towards reconstruction of the lost Late Bronze Age intra-caldera island of Santorini, Greece. Sci. Rep. 8, 548. https://doi.org/10.1038/s41598-018-25301-2.

Karlstrom, L., Dufek, J., Manga, M., 2009. Organization of volcanic plumbing through magmatic lensing by magma chambers and volcanic loads. J. Geophys. Res. 114, 937. https://doi.org/10.1029/2009JB006339.

Kennedy, B.M., Mark Jellinek, A., Stix, J., 2008. Coupled caldera subsidence and stirring inferred from analogue models. Nat. Geosci. 1, 385–389. https://doi.org/10.1038/ngeo206.

Konstantinou, K.I., Evangelidis, C.P., Liang, W.T., Melis, N.S., Kalogeras, I., 2013. Seismicity, Vp/Vs and shear wave anisotropy variations during the 2011 unrest at Santorini caldera, southern Aegean. J. Volcanol. Geotherm. Res. 267, 57–67. https://doi.org/10.1016/j.jvolgeores.2013.10.001.

Lipman, P.W., 1997. Subsidence of ash-flow calderas: relation to caldera size and magma-chamber geometry. Bull. Volcanol. 59, 198–218. https://doi.org/10.1007/s004450050186.

Ma, G.W., Hao, H., Wang, F., 2011. Simulations of explosion-induced damage to underground rock chambers. J. Rock Mech. Geotech. Eng. 3, 19–29. https://doi.org/10.3724/SP.J.1235.2011.00019.

Mainprice, D., 1997. Modeling the anisotropic seismic properties of partially molten rocks found at mid-ocean ridges. Tectonophysics 279, 161–179.

McClelland, E., Thomas, R., Hardy, D.A., 1990. A palaeomagnetic study of Minoan age tephra from Thera. In: Thera and the Aegean World III, Proceedings of the Third International Congress. The Thera Foundation, pp. 129–138.

Moser, T.J., 1991. Shortest path calculation of seismic rays. Geophysics 56, 59–67. https://doi.org/10.1190/1.1442958.

Muller, J.R., Ito, G., Martel, S.J., 2001. Effects of volcano loading on dike propagation in an elastic half-space. J. Geophys. Res. 106, 11101–11113. https://doi.org/10.1029/2000JB900461.

Nomikou, P., Druitt, T.H., Hubscher, C., Mather, T.A., Paulatto, M., Kalnins, L.M., Kelfoun, K., Papanikolaou, D., Bejelou, K., Lampridou, D., Pyle, D.M., Carey, S., Watts, A.B., Weiß, B., Parks, M.M., 2016a. Post-eruptive flooding of Santorini caldera (Greece), and implications for tsunami generation. Nat. Commun. 7, 1–22. https://doi.org/10.1038/ncomms13.

Nomikou, P., Hübscher, C., Ruhnau, M., Bejelou, K., 2016b. Tectono-stratigraphic evolution through successive extensional events of the Anydros Basin, hosting Kolumbo volcanic field at the Aegean Sea, Greece. Tectonophysics 671, 202–217. https://doi.org/10.1016/j.tecto.2016.01.021.

Nomikou, P., Parks, M.M., Papanikolaou, D., Pyle, D.M., Mather, T.A., Carey, S., Watts, A.B., Paulatto, M., Kalnins, M.L., Livanos, I., Bejelou, K., Simou, E., Perros, I., 2014. The emergence and growth of a submarine volcano: the Kameni islands, Santorini (Greece). GeoResJ 1–2, 8–18. https://doi.org/10.1016/j.grj.2014.02.002.

Papadimitriou, P., Kapetanidis, V., Karakonstantis, A., Kaviris, G., Voulgaris, N., Makropoulos, K., 2015. The Santorini Volcanic Complex: a detailed multiparameter seismological approach with emphasis on the 2011–2012 unrest period. J. Geodyn. 85, 32–57. https://doi.org/10.1016/j.jog.2014.12.004.

Parks, M.M., Caliro, S., Chiodini, G., Pyle, D.M., Mather, T.A., Berlo, K., Edmonds, M., Biggs, J., Nomikou, P., Raptakis, C., 2013. Distinguishing contributions to diffuse CO2 emissions in volcanic areas from magmatic degassing and thermal decarbonation using soil gas 222Rn–δ13C systematics: application to Santorini volcano, Greece. Earth Planet. Sci. Lett. 377–378, 180–190. https://doi.org/10.1016/j.epsl.2013.06.046.

Parks, M.M., Moore, J., Papanikolaou, X., 2015. From quiescence to unrest: 20 years of satellite geodetic measurements at Santorini volcano, Greece. J. Geophys. Res. 120. https://doi.org/10.1002/(ISSN)2169-9356.

Pfeiffer, T., 2001. Vent development during the Minoan eruption (1640 BC) of Santorini, Greece, as suggested by ballistic blocks. J. Volcanol. Geotherm. Res. 106, 229–242. https://doi.org/10.1016/S0377-0273(00)00273-0.

Pinel, V., Carrara, A., Maccaferri, F., Rivalta, E., Corbi, F., 2017. A two-step model for dynamical dike propagation in two dimensions: application to the July 2001 Etna eruption. J. Geophys. Res. 122, 1107–1125. https://doi.org/10.1002/2016JB013630.

Piper, D.J.W., Perissoratis, C., 2003. Quaternary neotectonics of the South Aegean arc. Mar. Geol. 198, 259–288. https://doi.org/10.1016/S0025-3227(03)00118-X.

Pyle, D.M., Elliott, J.R., 2006. Quantitative morphology, recent evolution, and future activity of the Kameni Islands volcano, Santorini, Greece. Geosphere 2, 253. https://doi.org/10.1130/GES00028.1.

Roche, O., Druitt, T.H., Merle, O., 2000. Experimental study of caldera formation. J. Geophys. Res. 105, 395–416. https://doi.org/10.1029/1999JB900298.

Sakellariou, D., Rousakis, G., Sigurdsson, H., Nomikou, P., Katsenis, I., Croff Bell, K.L., Carey, S., 2012. Seismic stratigraphy of Santorini's caldera: a contribution to the understanding of the Minoan eruption. In: Proc. 10th Hellenic Symposium on Oceanography & Fisheries, pp. 7–11.

Saltogianni, V., Stiros, S.C., Newman, A.V., Flanagan, K., Moschas, F., 2014. Time-space modeling of the dynamics of Santorini volcano (Greece) during the 2011–2012 unrest. J. Geophys. Res. https://doi.org/10.1002/2014JB011409.

Scandone, R., 1990. Chaotic collapse of calderas. J. Volcanol. Geotherm. Res. 42, 285–302. https://doi.org/10.1016/0377-0273(90)90005-Z.

Scandone, R., Acocella, V., 2007. Control of the aspect ratio of the chamber roof on caldera formation during silicic eruptions. Geophys. Res. Lett. 34. https://doi.org/10.1029/2007GL032059. L18314–4.

Sigurdsson, H., Carey, S., Alexandri, M., 2006. Marine investigations of Greece's Santorini volcanic field. Eos 87, 337–348.

Sparks, R., Wilson, C., 1990. The Minoan deposits: a review of their characteristics and interpretation. In: Thera and the Aegean World III, Proceedings of the Third International Congress. The Thera Foundation, pp. 89–99.

Stroujkova, A., 2018. Rock damage and seismic radiation: a case study of the chemical explosions in New Hampshire. Bull. Seismol. Soc. Am., 1–14. https://doi.org/10.1785/0120180117.

Tassi, F., Vaselli, O., Papazachos, C.B., Giannini, L., Chiodini, G., Vougioukalakis, G.E., Karagianni, E., Vamvakaris, D., Panagiotopoulos, D., 2013. Geochemical and isotopic changes in the fumarolic and submerged gas discharges during the 2011–2012 unrest at Santorini caldera (Greece). Bull. Volcanol. 75, 15. https://doi.org/10.1007/s00445-013-0711-8.

Taylor, M., Singh, S.C., 2002. Composition and microstructure of magma bodies from effective medium theory. Geophys. J. Int. 149, 15–21. https://doi.org/10.1046/j.1365-246X.2002.01577.x.

Toomey, D.R., Solomon, S.C., Purdy, G.M., 1994. Tomographic imaging of the shallow crustal structure of the East Pacific Rise at 9°30′N. J. Geophys. Res. 99, 24135–24157. https://doi.org/10.1029/94JB01942.

Tsampouraki-Kraounaki, K., Sakellariou, D., 2018. Seismic stratigraphy and geodynamic evolution of Christiana Basin, South Aegean Arc. Mar. Geol. 399, 135–147. https://doi.org/10.1016/j.margeo.2018.02.012.

Valentine, G.A., Graettinger, A.H., Sonder, I., 2014. Explosion depths for phreatomagmatic eruptions. Geophys. Res. Lett. 41, 3045–3051. https://doi.org/10.1002/2014GL060096.

Vanorio, T., 2005. Three-dimensional seismic tomography from Pwave and Swave microearthquake travel times and rock physics characterization of the Campi Flegrei Caldera. J. Geophys. Res. 110, 139. https://doi.org/10.1111/j.1365-246X.1980.tb02612.x.

Walker, G.P.L., 1984. Downsag calderas, ring faults, caldera sizes, and incremental caldera growth. J. Geophys. Res. 89, 8407–8416. https://doi.org/10.1029/JB089iB10p08407.

White, J.D.L., Ross, P.S., 2011. Maar-diatreme volcanoes: a review. J. Volcanol. Geotherm. Res. 201, 1–29. https://doi.org/10.1016/j.jvolgeores.2011.01.010.

Wilcock, W.S.D., Tolstoy, M., Waldhauser, F., Garcia, C., Tan, Y.J., Bohnenstiehl, D.R., Jacqueline Caplan-Auerbach, R.P.D., Arnulf, A.F., Mann, M.E., 2016. Seismic constraints on caldera dynamics from the 2015 Axial Seamount eruption. Science 354, 1395–1399. https://doi.org/10.1107/S0021889808042726.

Williams, H., 1941. Calderas and their origin. Univ. California Pub. Dept. Geol. Sci. 25, 239–346.

Wohletz, K.H., 2003. Water/Magma Interaction: physical considerations for the deep submarine environment. In: Explosive Subaqueous Volcanism. In: Geophysical Monograph Series. American Geophysical Union, Washington, DC, pp. 25–49.

Yokoyama, I., 1981. A geophysical interpretation of the 1883 Krakatau eruption. J. Volcanol. Geotherm. Res. 9, 359–378. https://doi.org/10.1016/0377-0273(81)90044-5.

Zandomeneghi, D., Barclay, A., Almendros, J., Ibañez Godoy, J.M., Wilcock, W.S.D., Ben-Zvi, T., 2009. Crustal structure of Deception Island volcano from Pwave seismic tomography: tectonic and volcanic implications. J. Geophys. Res. 114, B06310. https://doi.org/10.1029/2008JB006119.